IEEE TIM ID: # IM-20-01317

Title: Experimental Investigations into Bubble Characteristics in a Fluidized Bed through Electrostatic Imaging

Authors: Bojian Qi [a, b]

Yong Yan [c] (Corresponding author)

Wenbiao Zhang [a, b]

Xinyan Li [a, b]

Addresses: [a] State Key Laboratory of Alternate Electrical Power Systems with Renewable Energy Sources, North China Electric Power University, Beijing 102206, China

[b] School of Control and Computer Engineering, North China Electric Power University, Beijing 102206, China

[c] School of Engineering and Digital Arts, University of Kent, Canterbury, Kent CT2 7NT, U.K.

Tel: 00441227823015

Fax: 00441227456084

Email: y.yan@kent.ac.uk

ABSTRACT

Fluidized beds are widely applied in many industrial processes. In order to control and optimise the operation of a fluidized bed, it is necessary to develop reliable methods for the measurement of bubble characteristics to monitor the status of the bed. Electrostatic sensing methods based on the detection of charges on particles have been applied to characterize the particle motion in a fluidized bed. However, there is limited research on the measurement of bubble characteristics using the electrostatic methods due to complex electrostatic phenomena around the bubbles. In this paper, an imaging method using a two-dimensional electrostatic sensor array is employed for the experimental investigations into the bubble behaviors in a two-dimensional fluidized bed. The bubble size, shape, rising velocity and generation frequency are measured. Moreover, an optical imaging system is employed to obtain reference information to evaluate the performance of the electrostatic imaging method. Experimental results show that the bubble characteristics measured from the electrostatic sensor array have a good agreement with the results from the optical imaging system. The relative root mean square error between the bubble shapes measured from the electrostatic sensor array and from the optical system is 0.239 with a standard deviation within 4.7%.

Index Terms– Fluidized bed; electrostatic imaging; bubble characteristics; electrostatic sensor array; optical imaging system.

I. INTRODUCTION

Because of excellent heat and mass transfer characteristics, gas-solid fluidized beds are widely used in industrial processes ranging from chemical engineering, biomolecular engineering, and food processing. The excellent heat and mass transfer features, which are very important for improving product quality and reducing energy consumption, originate from the presence of bubbles in fluidized beds [1]. During the operation of a gas-solid fluidized bed, the gas moves upwards from the distributer and bubbles are gradually formed. The gas interacts with the solid particles, especially at the edges of the bubbles. The contact areas between the gas and the particles are large. Therefore, the heat and mass transfer between the gas and the solids is high and the reactants react intensively at the edges of the bubbles. Bubbles are easier to visualize than small particles. In addition, the characteristics of bubbles are closely related to the fluidization status, so reliable measurement of the bubble characteristics is desirable for the monitoring of the fluidization status and the optimisation of fluidized bed reactors. However, the behaviours of bubbles are complex, including upward movement, bursting and coalescence. Furthermore, there are opaque bed walls and intensive internal reactions in the fluidized bed. As a result, characterization of bubbles in a fluidized bed is challenging [2]. For example, there is still debate about the estimation of the bubble rising velocity [3].

Many researchers have studied the characteristics of the bubbles in a fluidized bed by means of several techniques [4]. These techniques are commonly classified as intrusive methods and non-intrusive methods. Pressure transducers and capacitive probes are intrusive to the process fluid. The size and frequency of the bubbles are determined from the fluctuations in the signals when the bubbles pass the sensing probe in sequence [5, 6]. However, the sensors in the intrusive methods disturb the movement of bubbles, so the measurement results are often inaccurate. Non-

intrusive measurement methods include primarily optical imaging [7], electrical capacitance tomography (ECT) [8], and magnetic resonance imaging (MRI) [9]. The optical imaging method requires a transparent window to access the fluidized bed and a delicate imaging system, it is therefore unsuitable for routine operations in a hostile industrial environment involving dust, high temperature and vibration. ECT is a "soft field" technology with its performance being limited by the number and size of electrodes in the system and is highly sensitive to the performance of the reconstruction algorithm. Moreover, the presence of electrostatic charge in the fluidized bed can affect adversely the operation of an ECT system and hence its reliability and accuracy [10]. MRI depends on the chemical composition of particles species and the bore size of the magnet in the apparatus [11]. In view of these disadvantages, the applicability of ECT and MRI to industrial fluidized beds is very limited. For this very reason a new non-intrusive imaging method is desirable to overcome the above drawbacks.

Electrostatic sensing is a non-intrusive technique with the potential to characterize the bubbles in a fluidized bed. In a gas-solid fluidized bed, triboelectric charging is inevitable due to the motion of particles which results in continuous particle-particle, particle-wall, and particle-fluid interactions [12, 13]. Electrostatic charge is induced on the electrode of an electrostatic sensor due to the movement of charged particles in the fluidized bed. The signal from the electrostatic sensor contains useful information about the particles. Electrostatic sensors have advantages of structural simplicity, passive detection, cost-effectiveness and robustness. For this reason, electrostatic sensing methods are widely used to investigate the flow dynamics and particle motions in a fluidized bed [14, 15]. However, previous research using electrostatic sensors focuses on the behaviors of particles. There is limited research on the measurement of bubble characteristics

through electrostatic sensing due to complex electrostatic phenomena around the bubbles and nonlinear and chaotic dynamics in a fluidized bed.

According to some experimental work performed on a fluidized bed, the movements of particles surrounding a rising bubble are more complex than those in an emulsion phase, resulting in stronger interactions among the particles and more charge is generated [16]. Therefore, the charge on the bubble edge distinguishes the bubble phase and the particle phase. The method of obtaining target images through electrostatic sensing and computation reconstruction of the target is called electrostatic imaging. Zhang *et al*. [17] used a wire-mesh electrostatic sensor to reconstruct the charge distribution of a cross-section of the fluidized bed. Nonetheless the wire-mesh electrostatic sensor is intrusive to the particles in the bed. Chen *et al*. [16] applied an iterative linear back-projection algorithm to the signals collected from four induction probes to reconstruct the charge distribution around a rising bubble in a gas-solid fluidized bed. However, the four probes are not enough to visualize many bubbles in the bed. Further research is required to develop an electrostatic sensor with an improved design for this purpose. Moreover, due to the complexity of the electrostatic characteristics at the bubble edge, the relationship between the charge reconstruction results obtained from the electrostatic sensing method and the bubble imaging remains to be explored. Once bubble images are obtained, the shape, size and rising velocity of the bubble may be determined by extracting the contour of the bubble. In addition to the time-domain analysis of the signals from electrostatic sensors, frequency-domain analysis should be conducted to measure the frequency of the bubble passage and identify the flow pattern in the bed.

Although some research has been conducted on the measurement of flow dynamics in a fluidized bed through electrostatic sensing, there is limited research on the measurement of bubble characteristics using electrostatic sensor arrays. In this paper, a novel imaging method is proposed

to acquire the bubble images in a fluidized bed through electrostatic sensing and image reconstruction. A novel 2D electrostatic sensor array with 4×8 electrodes is designed and then implemented on a laboratory-scale fluidized bed. Preliminary results of the charge reconstruction in the fluidized bed using the sensor array were first reported at the IEEE International Instrumentation Measurement Technology Conference in 2020 [18]. Experimental results show that the reconstructed charge distribution reflects the actual shape of the bubble. Based on the charge distribution measurement in the conference paper, the theoretical analysis and systematic experimental investigations of the bubble measurement through the electrostatic imaging have been conducted and are presented in detail in this paper. By reconstructing the charge distribution in the fluidized bed with a biharmonic spline interpolation algorithm, extracting the edge contours of the bubbles and analysing the frequency-domain information of the sensor signals, the bubble characteristics in the fluidized bed are measured and studied.

II. METHODOLOGY

A. General Principle

An electrostatic sensor array is installed on the wall of a gas-solid fluidized bed to measure the motion of bubbles in the bed. Fig. 1 shows the principle of the proposed electrostatic imaging method based on the electrostatic sensor array. The movement of charged particles in the bed is detected by the electrodes in the electrostatic sensor array due to electrostatic induction [18]. The fluctuations in the induced charge on the electrodes are converted into voltage signals through a signal conditioning unit and the signals are then fed into a data acquisition card. Signal processing methods are utilized to extract the information from the raw voltage signals both in the time and frequency domains. In the time domain analysis the root mean square (RMS) value of the voltage

signal from each electrode is calculated to represent the magnitude of the electrostatic charge. Charge distribution in the bed is reconstructed from the set of RMS values with a biharmonic spline interpolation algorithm [18]. The charge distribution in a fluidized bed is highly dependent on the spatial distribution of particles and bubbles. The movements of the particles around a rising bubble are more complex than that in a dense phase, resulting in more charge on particles [16]. Therefore, the charge on the bubble edge distinguishes the bubble phase from the particle phase. Once images of the charge distribution in the fluidized bed are obtained, the images are then processed to quantify the characteristics of the bubble, as shown in Fig. 1 (b). As a result, the bubble size, shape and rising velocity are determined. Moreover, the signals from the electrostatic sensor array are analysed in the frequency domain to measure the generation frequency of the bubble.

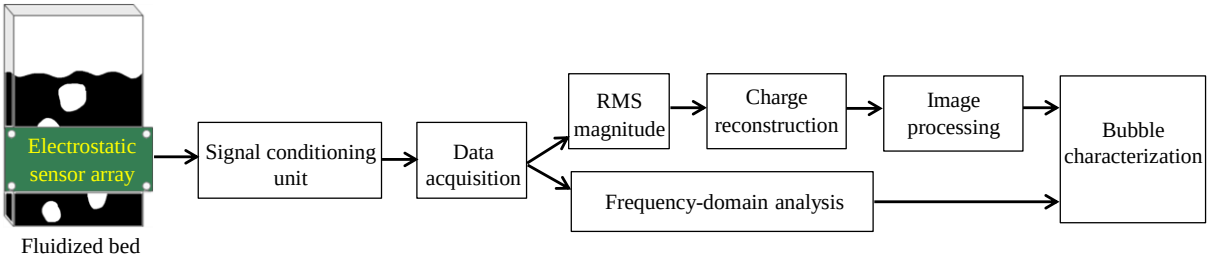

(a)

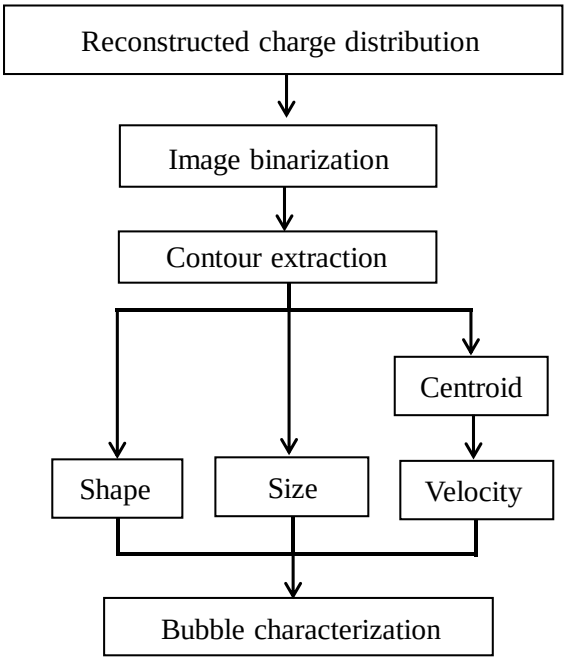

(b)

Fig. 1. Principle and structure of the electrostatic imaging system. (a) Block diagram. (b) Flow chart of the charge reconstruction and image processing.

B. Sensor Design and Signal Conditioning

The arrangement of the electrodes in the sensor array affects the sensitivity distribution of the sensor and hence the imaging accuracy. If a very limited number of electrodes are used to cover a given area of a fluidized bed, the measurement system will have a poor spatial resolution and low measurement accuracy. In contrast, if an exceedingly large number of electrodes are used, the size of each electrode will be very small and the spatial sensitivity of the electrode will be low in addition to the requirement of a complex signal conditioning unit and a time consuming reconstruction algorithm [19]. In the fluidized bed setup (Section 3), the diameters of the bubbles range mostly from 15 mm to 30 mm. In view of the characteristics of the bubbles and the sensitivity of the sensor, an electrostatic sensor array with 4×8 electrodes (i.e. four rows and eight columns) was designed and implemented in this study, as shown in Fig. 2. Each electrode

is 10 mm in length and 3 mm in width. It is worth mentioning that the bubbles mainly move in the axial direction in the bed, so the electrodes are set to have a strip type with a relatively short axial width to allow a wide signal bandwidth for the velocity measurement of the bubbles [20]. The electrodes are manufactured on the printed circuit board (PCB) with a thickness of 1 mm. The centre-to-centre spacing between the adjacent electrodes is 16 mm. The overall dimension of the sensing board (150 mm × 64 mm) is determined to cover the main section of the 2D bed. In order to minimize the external electromagnetic interferences, all areas around the electrodes (i.e. the green background in Fig. 2) are earthed.

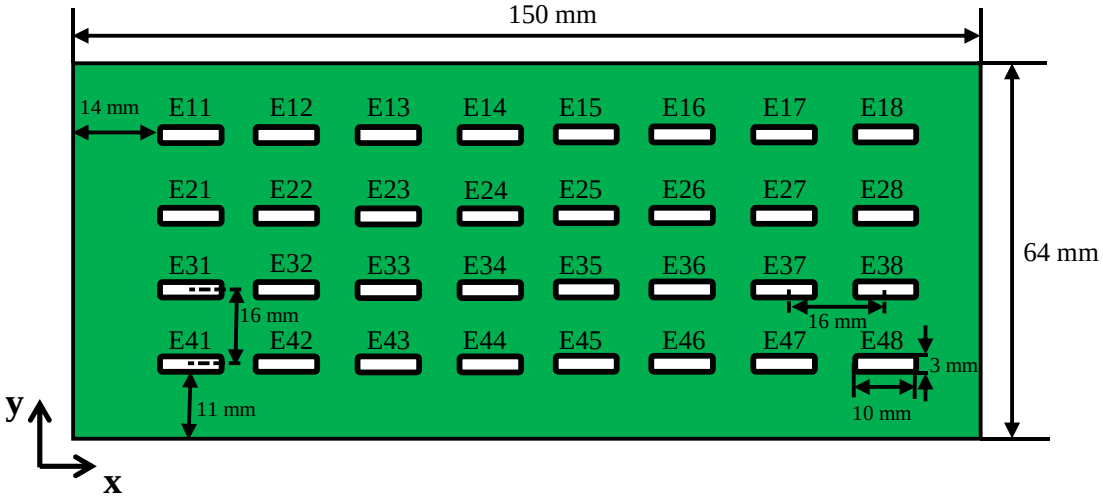

Fig. 2. Dimension and structure diagram of the electrostatic sensor array.

The sensitivity distribution of the electrostatic sensor array is quantified by modelling the electrostatic field of the array. Mathematical analysis and Finite Element Method (FEM) are common methods for electrostatic field modelling. Mathematical analysis is directly effective, but if assumptions are incorrect or the electrostatic field is complex, problems such as modelling errors or complex calculations will occur. FEM is a numerical analysis method to obtain approximate solutions of partial differential equations for engineering problems. FEM not only has high calculation accuracy, but also adapts to various complex structures, without being limited

by the shape of the field boundary. In view of the large number of electrodes in the sensor array, the sensitivity distribution of the sensor array is determined using the finite element software COMSOL, as shown in Fig. 3. A point charge with a net charge of 1 μC is considered as the source charge in the FEM modelling. The experimental setup (Section 3) is a pseudo two-dimensional bed with a bed thickness of 30 mm. As illustrated in Fig. 4 (a), the sensitivity distributions of the sensor array across the three representative planes of the bed thickness (labelled as Z1, Z2 and Z3, respectively) are calculated. Each plane is divided into a 150×64 grid with 1 mm between grid points and the charged particle is placed at the centre of different grid during the modelling. Moreover, the charge induced on each electrode is calculated through surface integration. The sensitivity of the n^{th} electrode is defined as:

$$S_n(x, y) = \frac{q_n}{q_s} \tag{1}$$

where q_n is the induced charge on the n^{th} electrode and q_s is the net charge of 1 μC.

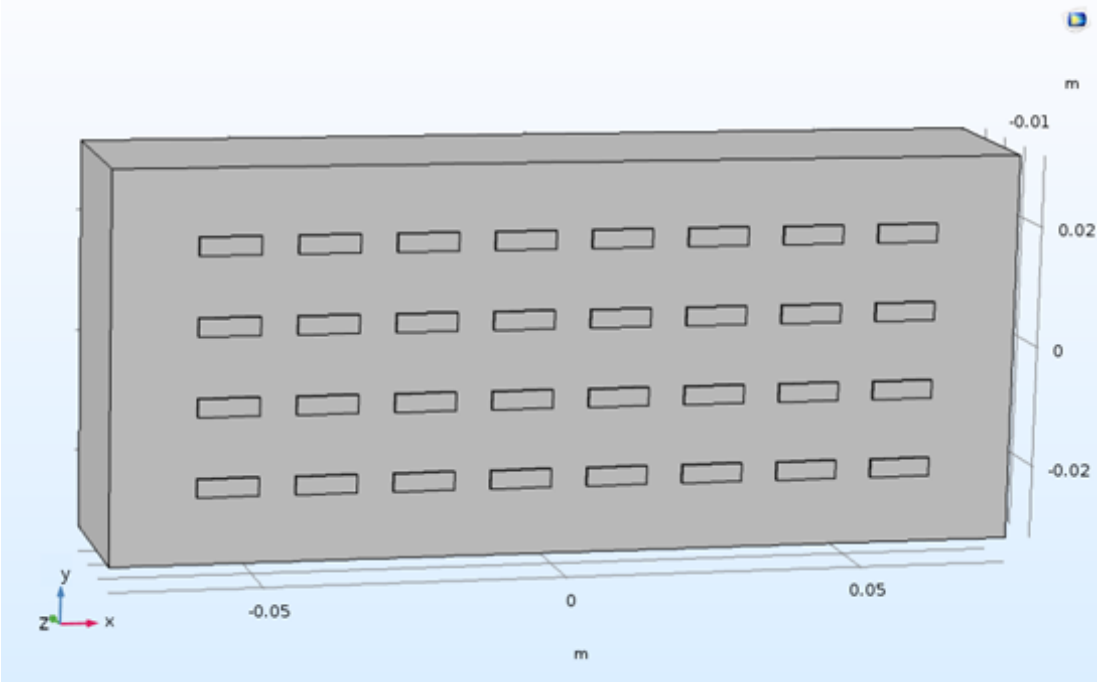

Fig. 3. FEM model of the sensor array.

The sensitivity of the array is calculated and shown in Fig. 4 (b)-(d). From the comparison of the sensitivity distributions across the three planes, the sensor array is more sensitive to charged particles near the electrode. The sensitivity decreases with the increase of the distance between the array and the sensing plane, and maximum sensitivities of the sensor array over the plane Z1, Z2 and Z3 are 0.127, 0.092 and 0.058, respectively. It should be noted that the thin fluidized bed with a thickness of 30 mm was used in this study to simplify the experimental work and the charged particles in the bed were located in a sensing zone of the sensor array. However, the sensing zone of the sensor array is limited due to the inherent limitation of electrostatic induction. In practice, it is necessary to optimise the design of the electrostatic sensor array according to the realistic dimensions of the fluidized bed. For instance, for a larger fluidized bed, the electrodes with larger size should be used to enhance the signal-to-noise ratio and extend the sensing zone [15, 21]. Additionally, it is found that the sensor array is more sensitive to the particles in the middle region of each plane. However, the bubbles to be detected in the bed are concentrated in the middle of the array and hence the non-uniform sensitivity near the edges of the array has little effect on the bubble measurement.

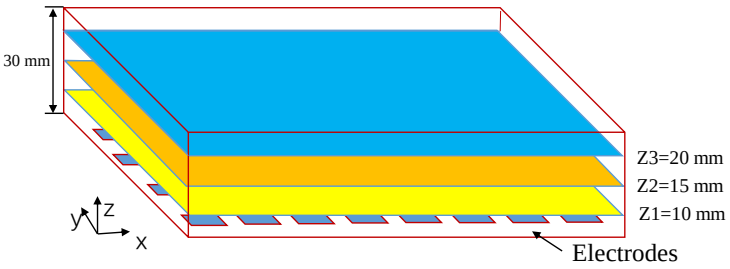

(a) Schematic diagram of the three planes.

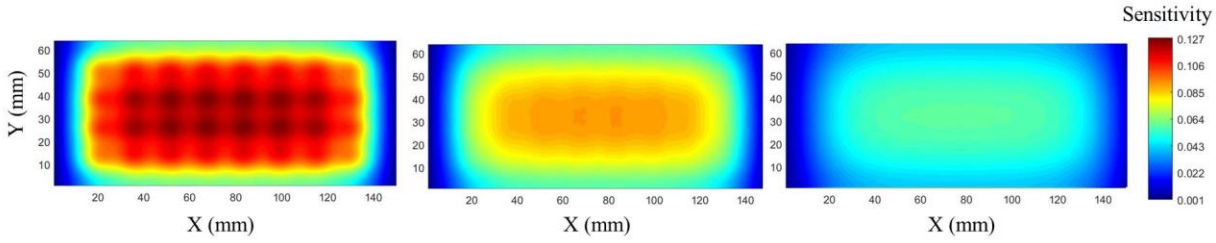

(b) Z1. (c) Z2. (d) Z3.

Fig. 4. Sensitivity distributions of the electrostatic sensor array across the three representative planes.

Apart from the sensor array, a multi-channel signal conditioning unit was also constructed in-house to filter and amplify the signals from the sensor array. A total of 32 signal conditioning circuits are made of PCB and covered with grounded shield cans, all of which are installed in an earthed metallic box in order to minimize external electromagnetic interference (Fig. 5). Each signal conditioning circuit consisting of three consecutive stages was built with operational amplifiers of LMP7721 and AD8602. With the movement of charged particles in the bed, the induced charge is generated on each electrode. A change of induced charge (i.e. induced current) is detected using the signal conditioning unit. The I/V converter in the signal conditioning unit firstly converts the weak current signal from the electrode into a voltage signal and completes the pre-amplification of the signal. When it comes to the second stage the voltage signal is further amplified using a secondary amplifier. In the third stage, the signal is then fed into a Salley-Key low-pass filter with a cut-off frequency of 1.6 kHz, which is appropriate for the dynamic response of the measurement system [17]. Eventually, a data acquisition card samples the 32 signals from the signal conditioning unit.

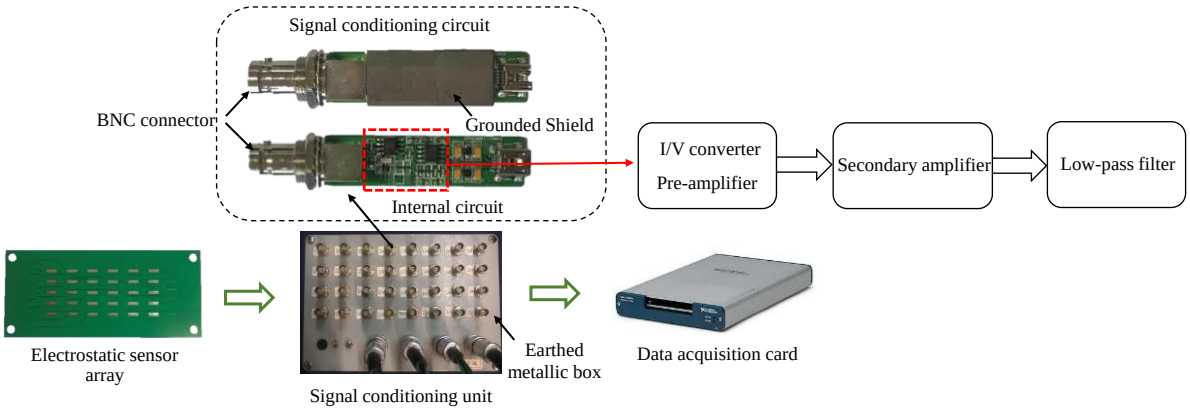

Fig. 5. Photograph of the signal conditioning unit.

C. Image Processing

The voltage signals from the electrostatic sensor array are further processed to obtain the image of the charge distribution in the fluidized bed. First of all, the RMS value of the signal from each electrode is calculated. Subsequently, a charge calibration process is conducted to determine the proportional coefficient between the induced charge and the RMS value of the signal. The charge calibration process has been reported in detail elsewhere [18]. Eventually, the charge distribution is reconstructed from the proportional coefficient and the set of RMS values with the biharmonic spline interpolation algorithm [18]. Once reconstructed images are created, image processing algorithms are then used to process the images to quantify the bubble characteristics. All the reconstruction and image processing were performed on a standard laptop PC with a 1 GHz Intel Core processor and 8 GB RAM. The biharmonic spline interpolation and image processing algorithms were developed in-house using MATLAB 2017, which take approximately 2.2 s to process one image. Extracting the bubble contour is the first step during the image processing. Fig. 6 (a) shows the contour extraction process. Firstly, greyscale images of the charge reconstruction are created by mapping the charge values to the grey levels. A threshold of the greyscale image is then determined using the Otsu method [22]. Secondly, the bubble contour is extracted by converting the greyscale image into a binary image. Finally, the greyscale image is converted into a pseudo colour image through pseudo colour scaling for purpose of visual presentation of the results. The jet colour map is adopted to map the grey level to a specific colour containing different red, green and blue intensities [18].

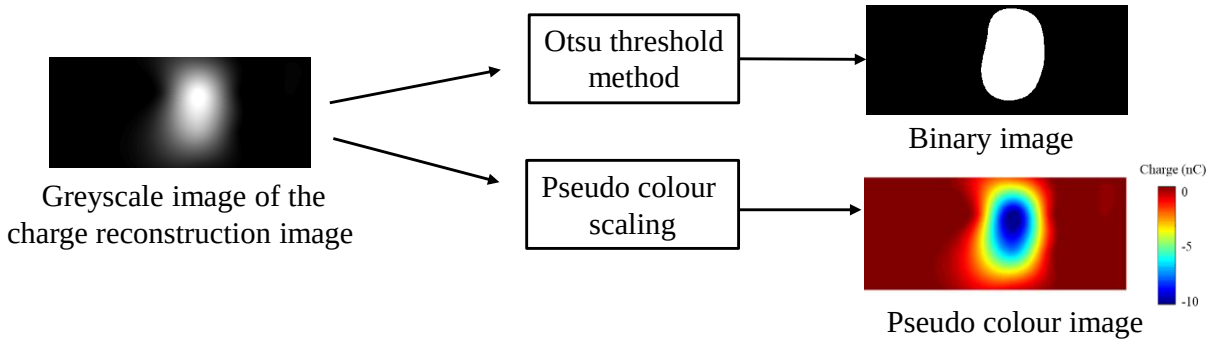

(a) Contour extraction.

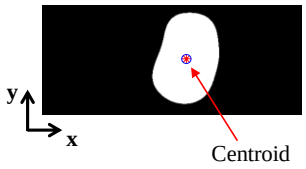

(b) Definition of the centroid.

Fig. 6. Contour extraction and definition of the centroid.

The Otsu method calculates the optimal threshold by separating the histogram of an image into two pixel groups (i.e. foreground and background groups) and ensures that the between-class variance is maximal. Firstly, all pixels of the greyscale image are viewed, and the number of occurrences of each pixel value is counted. Secondly, a pixel value is set as the threshold value for the current classification and all pixels are divided into two groups: foreground and background groups. Finally, the between-class variance V is determined from

$$V = w_0(s_0)w_1(s_0)[u_1(s_0) - u_0(s_0)]^2 \tag{2}$$

where u_0 and u_1 are the mean greyscales of foreground and background pixels, respectively. w_0 and w_1 are the probabilities of the pixels in the foreground and background groups, respectively. s_0 is the threshold value for the current classification.

When the between-class variance is the largest, the threshold at this time is used as the optimal threshold to distinguish the foreground from the background. Once the optimal threshold is determined, the reconstructed result is binarized, as given in Equation (3)

$$b(x,y)=\begin{cases}1, q(x,y)>s\\ 0, q(x,y)\le s\end{cases} \tag{3}$$

where b (x, y) is the value of each pixel in the binarized image, q (x, y) is the grey value of each pixel in the reconstructed grey image, and s is the optimal threshold. The Otsu method determines the optimal threshold and hence automatically segments the images. In this study, all pixels below the threshold are set to black, forming a particle phase, while all pixels above this threshold are set to white, indicating a gas phase. In addition to the bubble contour, a centroid of the bubble is marked in the image, as shown in Fig.6 (b). From the contour and the centroid information, a set of parameters including bubble size, shape and rising velocity are calculated.

Since a bubble is not always circular, its size is represented by the equivalent diameter of a circular bubble with the same cross-sectional area of the actual bubble. The equivalent diameter D is expressed as

$$D=\sqrt{\frac{4A}{\pi}} \tag{4}$$

where A is the area of the actual bubble, which is determined from counting the pixel number within the bubble contour (i.e. R) and the scale factor a between the pixel and the actual physical size.

$$A=a\sum_{(i,j)\in R}1 \tag{5}$$

The circularity C_r is used to describe the shape of the bubble, which is calculated from:

$$C_r=\frac{4\pi A}{P^2} \tag{6}$$

where P is the perimeter of the bubble contour. For a perfectly circular bubble, C_r is 1.

The bubble velocity is obtained by calculating the displacement of the centroids of bubbles from two adjacent images. The radial velocity v_x and axial velocity v_y of the bubble are calculated, respectively, as follows:

$$v_x = \frac{x_2 - x_1}{\Delta t} \tag{7}$$

$$v_y = \frac{y_2 - y_1}{\Delta t} \tag{8}$$

where, x_1 and y_1 are the coordinates of the bubble centroid in the first image, x_2 and y_2 are the coordinates of the bubble centroid in the second image, Δt is the time interval between the two adjacent images. Δt is determined from the sampling frequency of the sensor signal and the number of data to calculate each RMS value, which is set to 20 ms in this study.

III. EXPERIMENTAL RESULTS AND DISCUSSION

A. Experimental Setup

In order to measure the bubble characteristics using the electrostatic imaging method, a series of experiments was undertaken on a pseudo 2D gas-solid fluidized bed, as shown in Fig. 7. The 2D bed is made of Plexiglas with a height of 850 mm, a width of 150 mm and a thickness of 30 mm. Because of the 2D structure, changes of bubbles in the thickness direction are ignored. A rectangular nozzle with a size of 25 mm ×15 mm is fitted at the inlet of the bed to generate a series of stable bubbles. The air flow rate at the nozzle is regulated with a needle valve and measured with a rotameter (accuracy is 1.5%). In view of the convenience of installation, the electrode side of the electrostatic sensor array is closely mounted on outside of the fluidized bed wall and the other side is a grounded shielding layer. The relative permittivity of the bed wall is 3 and the thickness of the wall is 10 mm. It should be stressed that both the permittivity of the

material and the thickness of the wall affect the capacitance between the charged particles and the electrodes and hence the induced charge on the electrode. Therefore, for practical implementation, the inner surface of the sensor array should be mounted flush with the inner wall and the electrode should be insulated from the wall. In addition, the electrode should be covered with a wear-resistant insulating layer to avoid particle wear to the sensor. The centre of the sensor array is 100 mm above the distributor. A 32-channel signal conditioning unit was implemented for the acquisition of the signals from the sensor array at a sampling frequency of 1 kHz [18]. In addition, an optical imaging system with a digital camera (Fastcam Mini UX50) was placed on the back of the fluidized bed to capture the images of moving bubbles at a frame rate of 500 fps. The images from the camera are used to validate the results of the electrostatic imaging method. Fig. 7 shows the images of bubbles in upward movement with a time interval of 20 ms.

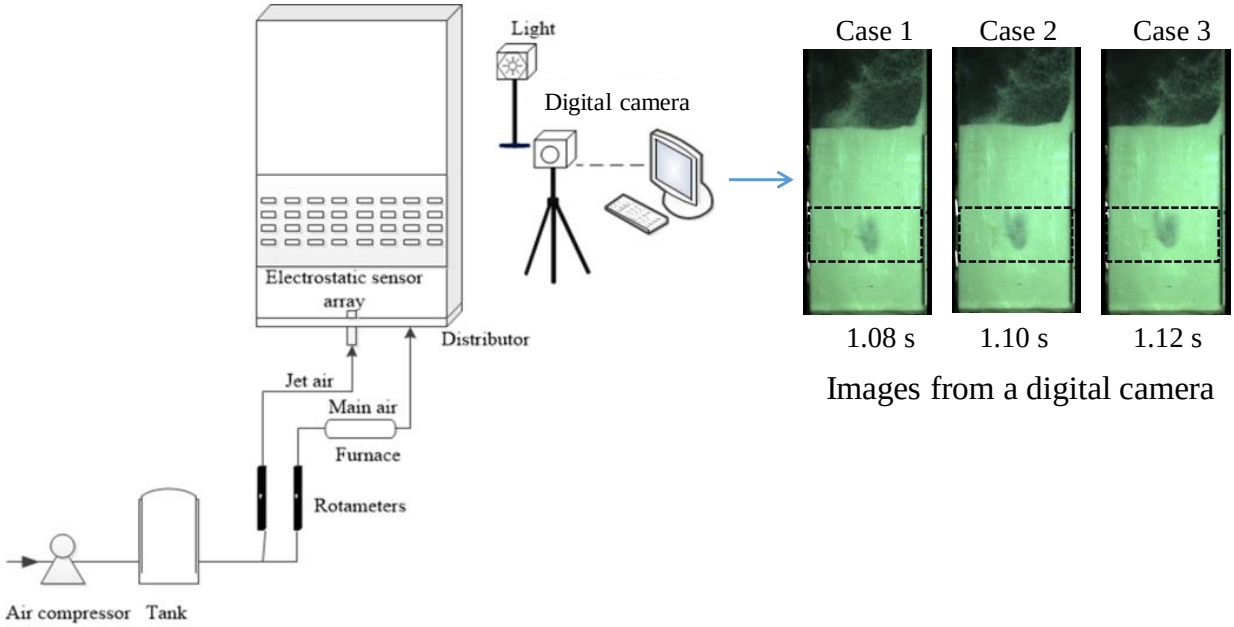

Fig. 7. Experimental setup and typical images from the digital camera.

B. Experimental Conditions

Glass beads with a diameter of 0.5 mm and a true density of 2440 kg/m^3 were used as test particles during the experiments. The glass beads are considered as Geldart B particles according to the Geldart diagram [23]. Before the start of the experiments, the initial bed height of the glass beads was set to 0.25 m. During the experiments the ambient temperature was 25℃ whilst the relative humidity was 60%, which were constant during the experiments. The glass beads were fluidized under five jet gas velocities, 3.96 m/s, 4.76 m/s, 5.56 m/s, 6.34 m/s and 7.14 m/s. The experiments were repeated for 3 times at each jet gas velocity and the total duration of the signals in each experiment is 10 s. Moreover, the standard deviation of the measurements from the repeated experiments is calculated. To maintain relatively stable bubbles at each jet gas velocity, the electrostatic sensor array and the digital camera started sampling simultaneously after the gas was injected for 10 s.

C. Results and Discussion

1) Validation Criteria

Quantitative evaluation criteria are used in this work to validate the electrostatic imaging method. The criteria include relative root mean square error (*RRMSE*), mean absolute error (*MAE*), correlation coefficient (*CORR*), which are defined as follows:

$$RRMSE = \left(\frac{\sum_{i=1}^{N} (b_i^* - b_i)^2}{\sum_{i=1}^{N} b_i^2} \right)^{0.5} \tag{9}$$

$$MAE = \frac{1}{N} \sum_{i=1}^{N} \left| b_i^* - b_i \right| \tag{10}$$

$$CORR = \frac{\sum_{i=1}^{N} (b_i - \overline{B})(b_i^* - \overline{B^*})}{\sqrt{\sum_{i=1}^{N} (b_i - \overline{B})^2 \sum_{i=1}^{N} (b_i^* - \overline{B^*})^2}} \tag{11}$$

Where b_i and b_i^* are the values of the i^{th} pixel in the binarized reference image B and binarized reconstructed image B^*, respectively. $\bar{B}$ and $\overline{B^*}$ are the mean intensity values of the matrices B and B^*, respectively. N is the total number of the pixels in the whole image. The *RRMSE* and *MAE* indicate the errors between the reconstructed and reference images, whilst the *CORR* shows the spatial similarity between them.

A typical example of the bubble in the bed at jet gas velocity 6.34 m/s is shown in Fig. 8. The bubble contours are detected using the digital camera and the electrostatic sensor array, respectively. The criteria are then calculated from the bubble contours.

Fig. 8. Images of a bubble at jet gas velocity 6.34 m/s. (a) Original image from the digital camera. (b) Binary image from the digital camera. (c) Image reconstructed from the electrostatic sensor array. (d) Binary image from the electrostatic sensor array.

By analysing the measurement results under different experimental conditions, the values of *RRMSE*, *MAE* and *CORR* are calculated. The average *RRMSE* between the results from the electrostatic imaging and the optical imaging is 0.239 with a standard deviation within 4.7%, and the average *MAE* is 0.0526 with a standard deviation within 1.6%. Therefore, the errors between the two imaging systems are small. The average *CORR* is 0.766 with a standard deviation within 5.6%, which shows the spatial similarity between the results from the two imaging methods is good. The above results demonstrate that the electrostatic imaging can well be applied to the measurement of the bubble contour in the fluidized bed with a reasonably high accuracy and a good repeatability.

2) Resolution of the Electrostatic Imaging

In order to measure the bubble characteristics, it is important to verify whether the electrostatic sensor array has sufficient resolution. The geometry of the sensor array and the characteristics of the signal processing circuit both affect the resolution of the electrostatic imaging. In an optical imaging system, the resolution is determined by the Rayleith criterion, which is defined as the distance of two close targets to be distinguished [24]. As a result, the imaging resolution of the electrostatic sensor array is considered as the distance between the edges of the two bubbles that can be distinguished in the measurement area. Two separated bubbles are used as close targets in the experiments to evaluate the resolution of the electrostatic sensor array, as shown in Fig. 9.

Fig. 9. Images of two bubbles. (a) Original image from the digital camera. (b) Corresponding binary image from the electrostatic sensor array.

Fig. 9 shows the results of two adjacent bubbles with the closest distance under the five different jet gas velocities ranging from 3.96 m/s to 7.14 m/s. The image processing algorithm is applied to obtain the right and left pixels of the adjacent bubbles, then the minimum distance between the edges of the bubbles (i.e. d_1) is calculated as 7.45 mm. In this case, the boundaries of each bubble are clearly separated. It is therefore estimated that the resolution of the proposed electrostatic imaging system is at least 7.45 mm. It is found from the optical imaging that the stable bubble diameter in the fluidized bed is between 15 mm to 30 mm. As a result, the

resolution of the electrostatic imaging system is sufficient to distinguish most of the bubbles in the present setup.

3) Measurement of Bubble Shape and Size

Based on the measurement principle in Section 2, the shape and size of the bubbles in the fluidized bed are measured using the electrostatic sensor array. During the process of the bubbles rising from the nozzle through the bed, the rising bubbles firstly coalesce with the surrounding small bubbles into large bubbles and then the large bubbles burst into small bubbles. In addition, the shapes of the bubbles change constantly. The bubbles appear in circular, elliptic, drop or irregular shapes. For jet gas velocities over the range of 3.96-7.14 m/s, experimental results show that there are four typical shapes of bubbles in the bed (Fig. 10). Table I lists the equivalent diameters and circularities of the bubbles which were detected using the electrostatic sensor array. Measurement of the bubble shape using the sensor array agrees well with the results from the digital camera. As shown in Fig. 10 (a), the bubbles are visible and all show a phenomenon of containing solids within them. The solids may be brought into a bubble by the jet that moves much faster than the bubble. Here only the contour of the bubble is of interest to us.

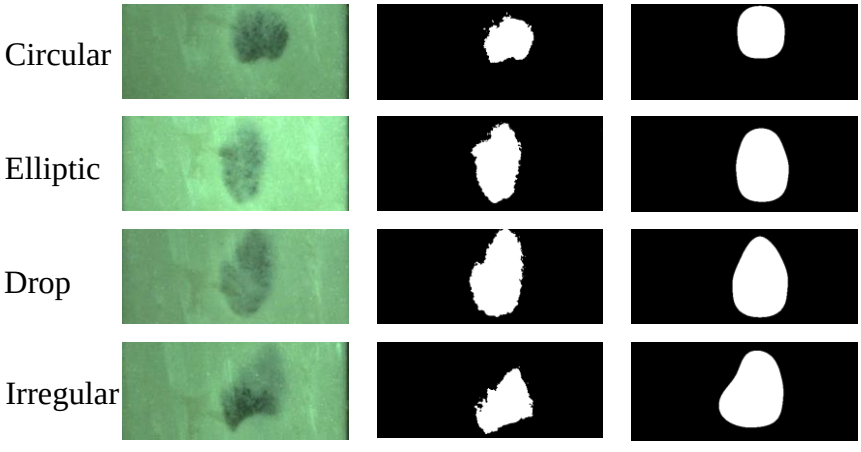

Fig. 10. Typical bubble shapes. (a) Original optical images from the digital camera. (b) Binary images from the optical digital camera. (c) Binary images from the electrostatic sensor array.

TABLE I

PARAMETERS OF BUBBLES

Bubble shape	Equivalent diameter (mm)	Circularity
Circle	17.09	0.91
Ellipse	20.90	0.86
Drop	21.98	0.83
Irregular shape	22.64	0.83

In addition, it is found that the bubble size depends on the jet gas velocity. In the experiments, the sensor array and the optical digital camera measure the bubbles simultaneously under the five different jet gas velocities. Fig. 11 depicts the mean equivalent diameter of the bubble measured with the electrostatic sensor array and the optical digital camera, respectively.

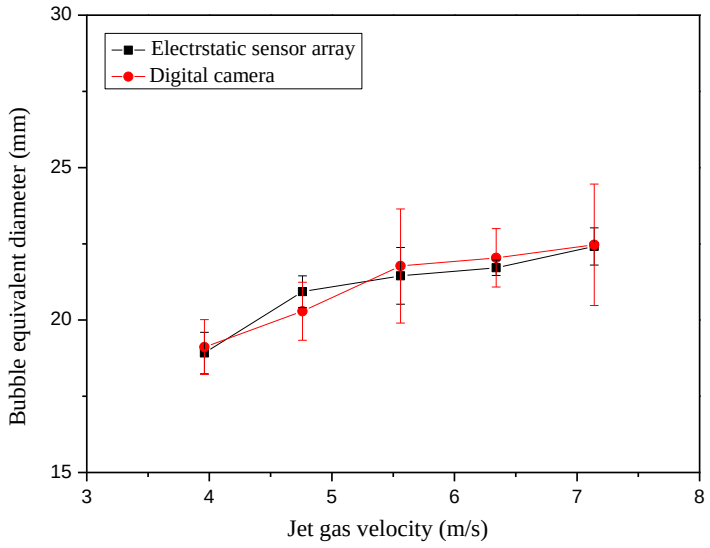

Fig. 11. Measurement of bubble sizes for different jet gas velocities.

Fig. 11 indicates that the mean equivalent diameter increases almost linearly with the jet gas velocity. This is because, with the increasing jet gas velocity, the increased gas volume, the expansion of the emulsion phase (i.e. the solids phase) and the coalescence of small bubbles eventually result in a larger bubble. However, the higher jet gas velocity also leads to bubble splitting, generating more small bubbles and consequently a wider variability of the bubble size. Moreover, the results of the bubble size from the electrostatic sensor array are very close to those from the digital camera. However, the standard deviation of the bubble size measured by the digital camera is greater than that from the electrostatic sensor array, suggesting that the fluctuations in the bubble size cannot be completely detected by the sensor array because of the relatively low spatial resolution. The resolution of the optical camera is 1280 (H) × 1024 (V). The image from the optical camera is cropped to obtain the image of the measurement area with a total of 379 (H) × 162 (V) pixels. According to the dimension of the measurement area (150 mm × 64 mm), the resolution of bubble measurement using the optical camera is 0.396 mm. Although the resolution of the electrostatic sensor array is relatively low, the sensor array is capable of imaging the bubble with a reasonably high accuracy.

4) Measurement of the Rising Velocity of the Bubble

Fig. 12 gives a series of bubble images from the electrostatic sensor array when the jet gas velocity varies from 3.96 m/s to 7.14 m/s. After the centroids of the bubbles are obtained from the two adjacent images, the radial and axial velocities of the bubble are determined.

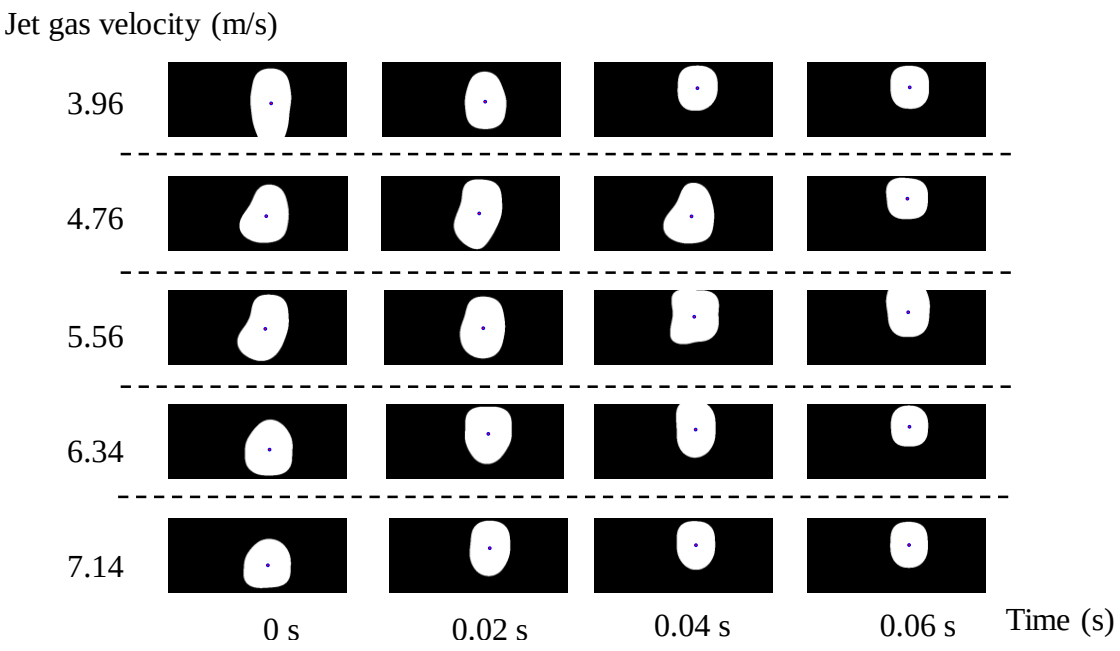

Fig. 12. Bubble images from the electrostatic sensor array for different jet gas velocities.

The velocity of the bubble depends on the jet gas velocity. Fig. 13 shows a comparison between the bubble velocity measured from the electrostatic sensor array and that from the digital camera. It can be seen from Fig. 13 (a) that the mean radial velocity of the bubble is no more than 0.2 m/s. In addition, no obvious relationship is observed between the mean radial velocity of the bubble and the jet gas velocity. The main reason for this is that the bubble grows or deforms due to the coalescence of the small bubbles after rising from the jet inlet, and the radial movement of the bubble is chaotic. Therefore, the axial velocity of the bubble is regarded as the rising velocity of the bubble.

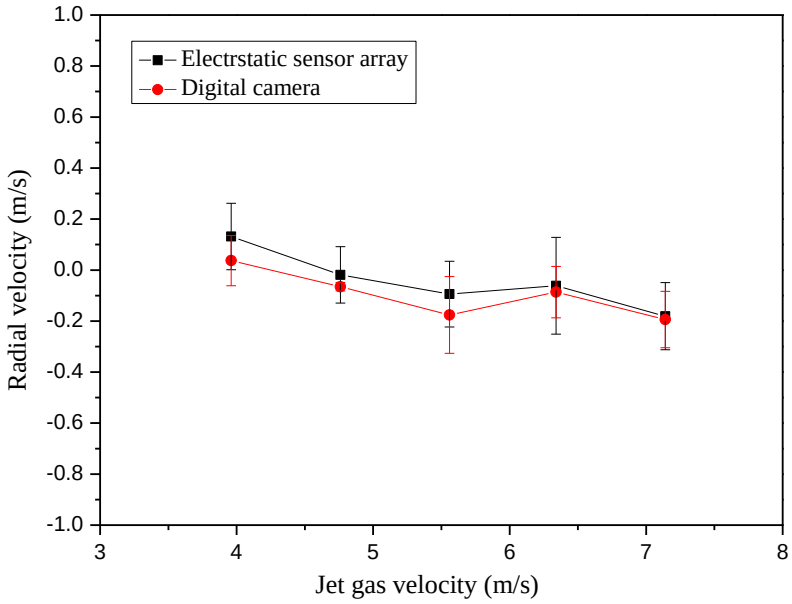

(a) Radial velocity.

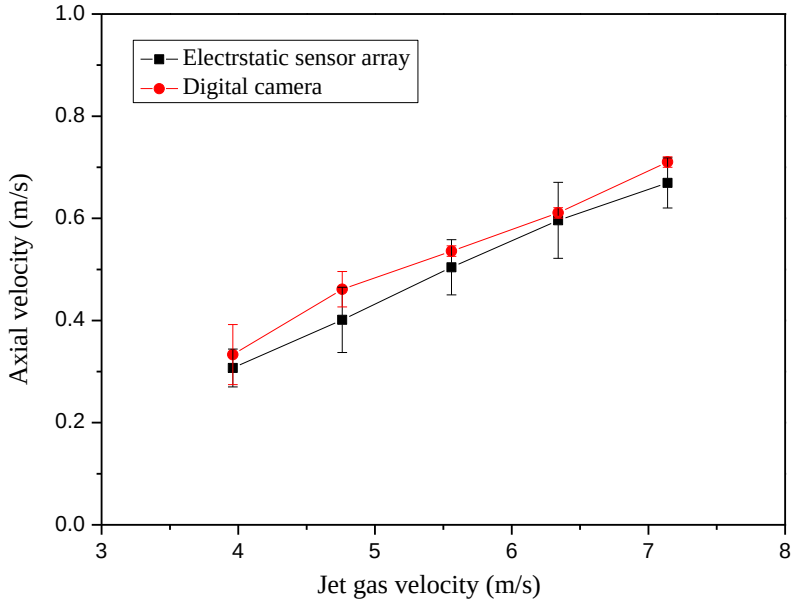

(b) Axial velocity.

Fig. 13. Measurement of bubble rising velocities for different jet gas velocities.

Even if the rising velocity of the bubble is affected by the coalescence and eruption of the bubbles [25], it still increases linearly with the jet gas velocity, as shown in Fig. 13 (b). The

bubble rising velocities measured from the electrostatic sensor array are very consistent with those from the digital camera. However, the average rising velocity from the optical digital camera is slightly higher than that from the sensor array. This is believed largely due to the low resolution of the electrostatic imaging method resulting in a smaller displacement of the centroids of bubbles in two adjacent images. In different fluidized bed reactors, the particle materials properties such as size, shape, density and chemical composition as well as operation conditions (i.e. jet gas velocity, humidity) may vary significantly [26], which influence the rising velocities of the bubbles. The experimental results show that the minimum rising velocities of the bubbles in the current fluidized bed measured from the electrostatic sensor array and the digital camera are 0.253 m/s and 0.255 m/s, respectively, when the jet gas velocity is 3.96 m/s.

5) Measurement of Bubble Generation Frequency

Through the analysis of a series of snapshots under five different jet gas velocities, three flow regions in the lateral direction of the fluidized bed are identified, i.e., one jet region in the middle of bed and two solid annulus regions near the walls [27]. The jet region is further subdivided into the jet formation zone, jet channel zone and bubble eruption zone along the axis direction of the bed. As shown in Fig. 14 (a) - (c), the Electrodes E45, E35 and E15 in the sensor array are close to the regions from the jet formation zone, jet channel zone and bubble eruption zone respectively. The result from Electrode E25 is very close to that from E35 and hence not discussed separately. During the fluidized bed operation, the bubbles generated by the high-velocity jet entrain the solid particles into the jet formation zone and moved upward along the jet channel zone. The bubble generation frequency reflects the reaction and fluidization status in the bed, so it is desirable to monitor the bubble generation frequency. In previous studies [5, 7], the power spectral density (PSD) function is one of the most commonly used methods in the

frequency-domain analysis of the signals from gas-solids fluidized beds. The dominant frequency derived from the PSD is effective in characterizing the bubble behaviours. Therefore, the PSD functions derived from the signals from the electrostatic sensor array are analysed in this study to obtain the bubble generation frequency.

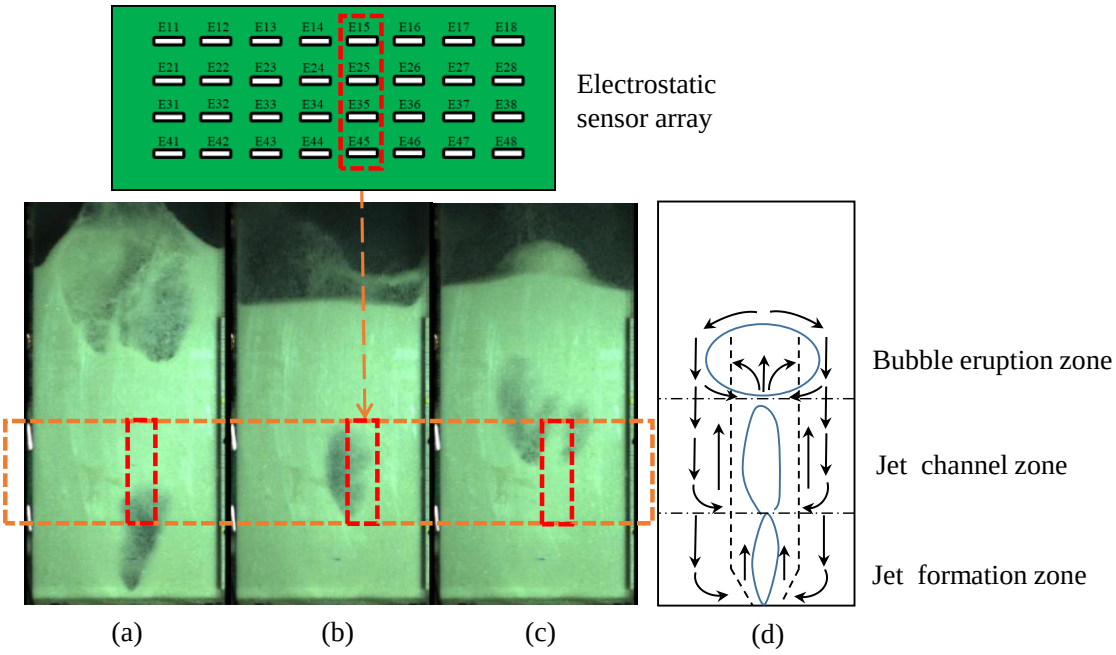

Fig. 14. Typical flow regions in the fluidized bed. (a) Jet formation zone. (b) Jet channel zone. (c) Bubble eruption zone. (d) Schematic diagram of the flow region.

Fig. 15 presents the normalized PSD of the signals from the electrostatic sensor array under different jet gas velocities. The frequency of signal oscillations is an indication of the bubble generation frequency. The normalized PSD from Electrode E15 (Fig. 15 (a)) shows that wider spectral bands exist and the signals are unstable. The reason is that E15 is located in the bubble eruption zone where the flow behaviour is the most unstable. Moreover, the dominant frequency of the signal from E15 increases with the jet gas velocity, because more bubbles are erupted with a greater jet gas velocity.

Fig. 15 (b) suggests that the wide spectral band from Electrode E35 appears when the jet gas velocity is greater than 4.76 m/s. With an increasing jet gas velocity, the signal from Electrode E35 has a sharper peak in the spectrum. The dominant frequency increases with the jet gas velocity and stays within 7.6 Hz - 8.2 Hz. The reason is that E35 is located in the jet channel zone where bubbles mainly flow upwards in this area. The jet gas velocity affects significantly the bubble generation frequency when the jet gas velocity is low. When the jet gas velocity increases, the fluidization, bubble coalescence and bubble formation tend to be more stable. The bubble generation frequency is little affected by the jet gas velocity when the jet gas velocity is high.

The signals from the lower electrode E45 contain sharp (i.e. narrow band) peaks in the spectra. It can be seen from Fig. 15 (c) that the dominant frequency of the signal from Electrode E45 is around 7.8 Hz when the jet gas velocity varies from 4.76 m/s to 7.14 m/s. Since Electrode E45 is close to the jet formation zone, bubbles are formed continuously at this position and the bubble generation frequency is stable. In summary, the frequency-domain analysis of the signals from the electrostatic sensor array has revealed some fluid dynamics in the fluidized bed.

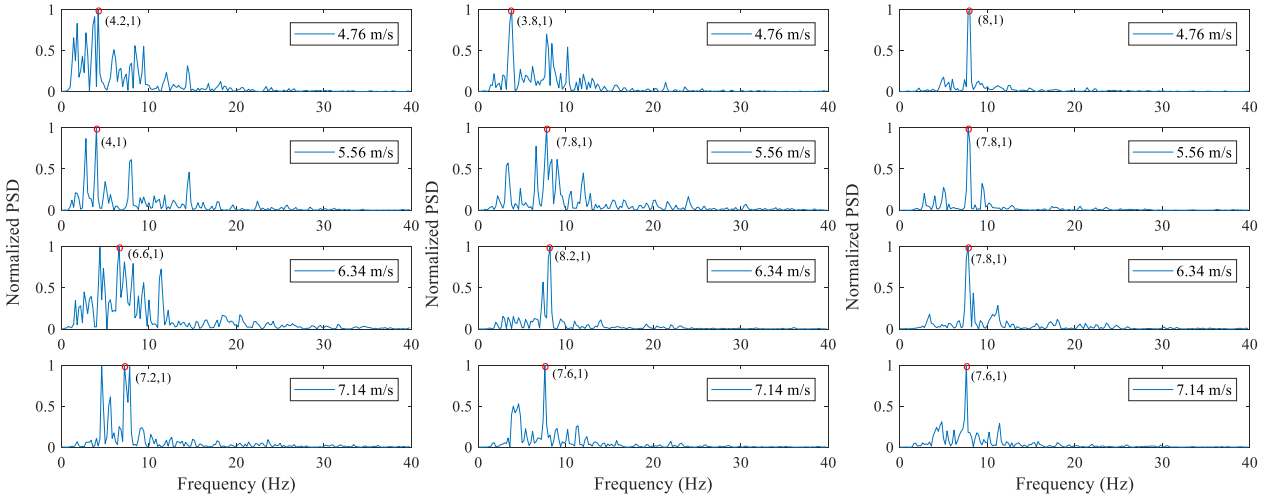

(a) E15 (b) E35 (c) E45

Fig. 15. PSD of the signals from Electrodes E15, E35 and E45.

IV. CONCLUSION

In this paper, an imaging method for measuring bubble characteristics using an electrostatic sensor array has been presented, with the support of analytical and experimental results. Four parameters have been measured from the signals, which are the bubble size, shape, rising velocity and generation frequency. The results have demonstrated that the electrostatic imaging method can determine the bubble contour in the fluidized bed. The method has been validated with reference to the conventional optical imaging results. The resulting average *RRMSE*, *MAE* and *CORR* between the reconstructed image and the reference image are 0.239, 0.0526 and 0.766, respectively. Furthermore, it has been proved that the electrostatic sensor array is capable of measuring the bubble generation frequency and distinguishing the jet formation zone, jet channel zone and bubble eruption zone in the fluidized bed. This is achieved by analysing the width of the power spectrum of the signal from the sensor array and the dominant frequency. The experimental results have shown that with the increasing jet gas velocity in the fluidized bed, the size and rising velocity of the bubbles become larger and the bubble generation frequency tends to be more stable. It should be stressed that the resolution of the proposed electrostatic imaging system with a sensor array of 32 10 mm × 3 mm strip electrodes has also been determined, which is 7.45 mm. Although this resolution is lower than that of the optical imaging (0.396 mm), the electrostatic imaging for measuring bubbles has a high accuracy. The resolution of the electrostatic imaging technique will be improved if more electrodes are used in the array.

Although the experimental investigations in this paper were conducted on a 2D fluidized bed, the proposed method has a potential to be deployed for the bubble characterization on a 3D fluidized bed.

ACKNOWLEDGMENT

The authors wish to acknowledge the National Natural Science Foundation of China (No. 61403138) and Beijing Natural Science Foundation (No. 3202028) for providing financial support.

REFERENCES

[1] T. Wang, Z. Xia, C. Chen, Coupled CFD-PBM simulation of bubble size distribution in a 2D gas-solid bubbling fluidized bed with a bubble coalescence and breakup model, Chem. Eng. Sci. 202 (2019) 208–221.

[2] T. Chandrasekera, Y. Li, D. Moody, M. Schnellmann, J. Dennis, D. Holland, Measurement of bubble sizes in fluidised beds using electrical capacitance tomography, Chem. Eng. Sci. 77 (2015) 679-687.

[3] C. Müller, J. Davidson, J. Dennis, P. Fennell, L. Gladden, A. Hayhurst, M. Mantle, A. Rees, A. Sederman, Rise velocities of bubbles and slugs in gas-fluidised beds: ultra-fast magnetic resonance imaging, Chem. Eng. Sci. 62 (2007) 82–93.

[4] J. Sun, Y. Yan, Non-intrusive measurement and hydrodynamics characterization of gas–solid fluidized beds: a review, Meas. Sci. Technol. 27 (2016) 112001.

[5] J. Werther, Measurement techniques in fluidized beds, Powder Technol. 102 (1999) 15–36.

[6] K. Nosrati, S. Movahedirad, M. Sobati, A. Sarbanha, Experimental study on the pressure wave attenuation across gas-solid fluidized bed by single bubble injection, Powder Technol. 305 (2017) 620–624.

[7] S. Movahedirad, A. Dehkordi, M. Banaei, N. Deen, M. Annaland, J. Kuipers, Bubble size distribution in two-dimensional gas-solid fluidized beds, Ind. Eng. Chem. Res. 51 (2012) 6571–6579.

[8] X. Li, A. J. Jaworski, X. Mao, Comparative study of two non-intrusive measurement methods for bubbling gas-solids fluidized beds: electrical capacitance tomography and pressure fluctuations, Flow Meas. and Instrum. 62 (2018) 255–268.

[9] A. Penn, C. M. Boyce, K. Pruessmann, C. Müller, Regimes of jetting and bubbling in a fluidized bed studied using real-time magnetic resonance imaging, Chem. Eng. J. 383 (2020) 123185.

[10] W. Zhang, C. Wang, W. Yang, C. Wang, Application of electrical capacitance tomography in particulate process measurement – A review, Adv. Powder Technol. 25 (2014) 174–188.

[11] M. Pore, D. Holland, T. Chandrasekera, C. Müller, A. Sederman, J. Dennis, L. Gladden, J. Davidson, Magnetic resonance studies of a gas–solids fluidised bed: Jet–jet and jet–wall interactions, Particuology 8 (2010) 617–622.

[12] F. Fotovat, X. Bi, J. Grace, Electrostatics in gas-solid fluidized beds: A review, Chem. Eng. Sci. 173 (2017) 303-334.

[13] F. Fotovat, X. Bi, J. Grace, A perspective on electrostatics in gas-solid fluidized beds: Challenges and future research needs, Powder Technol. 329 (2018) 65–75.

[14] Y. Yang, Q. Zhang, C. Zi, Z. Huang, W. Zhang, Z. Liao, J. Wang, Y. Yang, Y. Yan, G. Han, Monitoring of particle motions in gas-solid fluidized beds by electrostatic sensors, Powder Technol. 308 (2017) 461–471.

[15] W. Zhang, Y. Yan, Y. Yang, J. Wang, Measurement of flow characteristics in a bubbling fluidized bed using electrostatic sensor arrays, IEEE Trans. Instrum. and Meas. 65 (2016) 703-712.

[16] A. Chen, X. Bi, J. Grace, Charge distribution around a rising bubble in a two-dimensional fluidized bed by signal reconstruction, Powder Technol. 177 (2007) 113-124.

[17] W. Zhang, Y. Yan, X. Qian, Y. Guan, K. Zhang, Measurement of charge distributions in a bubbling fluidized bed using wire-mesh electrostatic sensors, IEEE Trans. Instrum. and Meas. 66 (2017) 522-534.

[18] B. Qi, W. Zhang, Y. Yan, X. Li, Continuous measurement of charge distribution in a single-jet fluidized bed using an electrostatic sensor array, in Proc. IEEE Instrum. Meas. Technol. Conf. Dubrovnik, Croatia, May 2020.

[19] X. Qian, Y. Yan, X. Huang, Y. Hu, Measurement of the mass flow and velocity distributions of pulverized fuel in primary air pipes using electrostatic sensing techniques, IEEE Trans. Instrum. and Meas. 66 (2017) 944-952.

[20] Y. Hu, Y. Yan, X. Qian, W. Zhang, A comparative study of induced and transferred charges for mass flow rate measurement of pneumatically conveyed particles, Powder Technol. 356 (2019) 715–725.

[21] C. Xu, S. Wang, G. Tang, D. Yang, B. Zhou, Sensing characteristics of electrostatic inductive sensor for flow parameters measurement of pneumatically conveyed particles, J. Electrost. 65 (2007) 582–592.

[22] Y. Zhao, S. Liu, Z. Hu, Y. Bai, C. Shen, X. Shi, Separate degree based Otsu and signed similarity driven level set for segmenting and counting anthrax spores, Comput. Electron. Agr. 169 (2020) 105230.

[23] D. Geldart, Types of gas fluidization, Powder Technol. 7 (1973) 285–292.

[24] Q. Xie, Y. Jiang, J. Liang, E. Qu, L. Ren, Incoherent, non-invasive and non-scanning superoscillation-based microscope for super-resolution imaging, Opt. Commun. 463 (2020) 125445.

[25] S. Shrestha, J. Gan, Z. Zhou, Micromechanical analysis of bubbles formed in fluidized beds operated with a continuous single jet, Powder Technol. 357 (2019) 398–407.

[26] C. Agu, L. Tokheim, M. Eikeland, B. Moldestad, Improved models for predicting bubble velocity, bubble frequency and bed expansion in a bubbling fluidized bed, Chem. Eng. Res. Des. 141 (2018) 361–371.

[27] K. Zhang, B. Yu, J. Chang, G. Wu, T. Wang, D. Wen, Hydrodynamics of a fluidized bed co-combustor for tobacco waste and coal, Bioresour. Technol. 119 (2012) 339–348.